Interfacial stress analysis and prediction of debonding for a thin plate bonded to a curved substrate

Laura de Lorenzis, Giorgio Zavarise

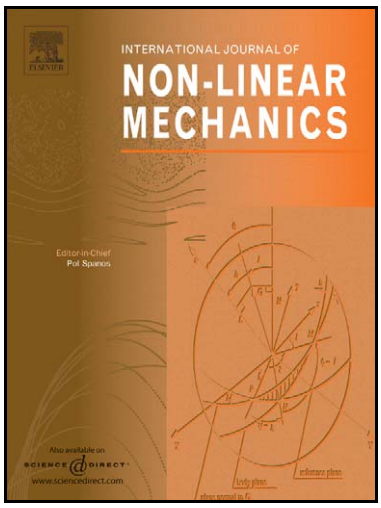

www.elsevier.com/locate/nlm

Interfacial stress analysis and prediction of debonding for a thin plate bonded to a curved substrate

Laura De Lorenzis, Giorgio Zavarise

PII: S0020-7462(09)00012-2
DOI: doi:10.1016/j.ijnonlinmec.2009.01.002
Reference: NLM 1574

To appear in: *International Journal of Non-Linear Mechanics*

Received date: 12 July 2008
Revised date: 9 December 2008
Accepted date: 9 January 2009

Cite this article as: Laura De Lorenzis and Giorgio Zavarise, Interfacial stress analysis and prediction of debonding for a thin plate bonded to a curved substrate, *International Journal of Non-Linear Mechanics* (2009), doi:10.1016/j.ijnonlinmec.2009.01.002

Interfacial stress analysis and prediction of debonding for a thin plate bonded to a curved substrate

Laura De Lorenzis, Giorgio Zavarise
Department of Innovation Engineering, Università del Salento
Via per Monteroni, 73100 Lecce, ITALY
laura.delorenzis@unile.it, giorgio.zavarise@unile.it

Keywords: bond, cohesive zone modeling, contact mechanics, curved substrate, debonding, fiber-reinforced polymer reinforcement, finite element method, interfacial stresses

ABSTRACT

This paper focuses on the analytical and numerical modeling of the interface between a rigid substrate with simple constant curvature and a thin bonded plate. The interfacial behavior is modeled by independent cohesive laws in the normal and tangential directions, coupled with a mixed-mode fracture criterion. The newly developed analytical model determines the interfacial shear and normal stress distributions as functions of the substrate curvature, during the various behavioral stages of the interface prior to the initiation of debonding. The model is also able to predict the debonding load and the effective bond length. In the numerical model the interface is modeled by zero-thickness node-to-segment contact elements, in which both the geometrical relationships between the nodes of the discretized problem and the interface constitutive laws are suitably defined. Numerical results and comparisons between the predictions of the two models are presented.

1. INTRODUCTION

The mechanics of interfacial bond between a thin plate and a flat quasi-brittle substrate under mode-II loading has been extensively studied (Chen and Teng 2001, De Lorenzis et al. 2001, Yuan et al. 2004, Ferracuti et al. 2006). These investigations have clarified the whole range of response of a bonded joint subjected to predominant shear stresses, starting from the linear elastic stage, up to the final debonding. A typical example is given by fiber-reinforced polymer (FRP) strips bonded to concrete or masonry.

Quite surprisingly, very limited attention has been focused on structural members with a curved surface, despite the fact that such members are often found in practice (De Lorenzis et al. 2006). The strengthening of a masonry arch with FRP strips to inhibit the formation of hinges constitutes a typical example (De Lorenzis 2008). In this case, the interfacial normal stresses are related by equilibrium to the interfacial shear stresses, and result tensile for concave substrates (e.g. intrados of an arch) and compressive for convex substrates (e.g. extrados of an arch) (Figure 1). If the FRP strip is placed at the intrados, the interfacial normal (peeling) tensile stresses are likely to lead to mixed-mode fracture of the masonry substrate, and thus to accelerate debonding with respect to the mode-II fracture case (Aiello et al. 2004, CNR 2004, Foraboschi 2004). Debonding phenomena have been observed in several experiments on arches strengthened at the intrados, so that the use of anchoring devices as preventive measures has been proposed (Eshwar et al. 2003, De Lorenzis et al. 2007). However, neither analytical nor numerical approaches have been proposed so far to tackle the problem from a mechanical standpoint.

This paper is devoted to the analytical and numerical modeling of the interface between a rigid substrate with simple constant curvature and a thin bonded plate. The interfacial

behavior is modeled by independent bilinear cohesive laws in the normal and tangential directions, coupled with a mixed-mode fracture criterion. The newly developed analytical model, based on equilibrium and compatibility relationships and making use of appropriate simplifying assumptions, permits to determine the interfacial shear and normal stress distributions along the bond length as functions of the substrate curvature, during the various behavioral stages of the interface prior to the initiation of debonding. The evolution of the interface from the initial stage of loading up to the onset of debonding can thus be examined. The model is also capable of predicting the debonding load and the effective bond length of the interface. The numerical model describes the interfacial behavior using zero-thickness node-to-segment contact elements, in which both the geometrical relationships between the nodes of the discretized problem and the interface constitutive laws are suitably defined. The predictions of the analytical and numerical models in terms of interfacial stress distributions, load vs. loaded-end displacement curves and debonding load are analyzed as functions of the substrate curvature.

2. ANALYTICAL COHESIVE ZONE MODELING OF THE INTERFACIAL STRESSES

2.1. Problem definition

The model considers a thin plate of thickness t, unit width and length L, made of a linearly elastic material with elastic modulus E. The plate is bonded to a rigid substrate with a constant in-plane curvature radius r and loaded with a force F (Figure 2a). The substrate curvature is such that the normal stresses arising at the interface are tensile, as will be shown later. The force direction is tangent to the substrate surface at the loaded end. A curvilinear coordinate with origin at the plate free end, s, is introduced, and the corresponding polar coordinate is $\theta = s/r$. The interfacial stresses can be equivalently expressed as functions of s or θ.

Figure 2b shows a differential element of the plate. Due to the small thickness, both the bending and shear stiffnesses of the plate are neglected, therefore only axial forces are considered. The circumferential stress in the plate is denoted as σ_θ. Normal and tangential stresses, p_N and p_T, arise at the interface between the plate and the substrate. Both stresses are considered uniform across the thickness of the adhesive layer, hence equal and opposite stresses are transmitted to the upper surface of the substrate.

2.2. Cohesive zone modeling

Due to its simplicity, cohesive zone modeling is largely used for a variety of applications, including fracture of ductile and brittle solids, delamination in composites at the micro- or macro-scale, and behaviour of adhesive layers. Different approaches have been used in the literature for cohesive zone modeling of interfaces under mixed-mode conditions (De Lorenzis and Zavarise 2008):

a. *Uncoupled cohesive zone modeling*. In this approach, the cohesive laws in the normal and tangential directions (i.e., respectively, the mode-I and mode-II cohesive laws) are independent from each other. This approach was used by Kafkalidis and Thouless (2002), and Li et al. (2006), among others. The energy release rates in mode I (G_I) and mode II (G_{II}) are identified as the areas under the respective cohesive laws. The total energy release rate is the sum of G_I and G_{II}. A further distinction can be made between approaches in which:

a1. A mixed-mode failure criterion is introduced, see e.g. Kafkalidis and Thouless (2002), and Li et al. (2006). Once the failure condition is reached, the element is considered no longer capable to bear any load. This assumption yields sudden drops in the tractions before the critical separation is reached. Nevertheless, this approach was shown to provide good capabilities to capture essential properties of adhesive joints.

a2. No mixed-mode fracture criterion is introduced. In this case, failure is assumed when either G_I or G_{II} reach their respective maximum values.

b. *Coupled cohesive zone modeling*. In this approach, the cohesive laws in the normal and tangential directions are linked together, typically by means of a coupling parameter. Also in this case a further distinction can be made between approaches in which:

b1. The cohesive laws are derived from a potential. A frequently used coupled cohesive law of this type is that developed by Tvergaard (1990), which uses a dimensionless coupling parameter between the normal and tangential laws. With this approach, the fracture energy is the same in all mode mixities. This is often regarded as a drawback, as the experimental evidence indicates the fracture energy to be often significantly larger in mode II than in mode I (Högberg 2006).

b2. The cohesive laws are not derived from a potential. Laws of this type have been proposed by Xu and Needleman (1993), and Högberg (2006), among others. These laws allow for different fracture energies in different mode mixities. Also, the lack of a potential introduces a path-dependency, which has a physical ground considering that cohesive zone models can describe an irreversible damage process at an interface (van den Bosch et al. 2006).

In this paper two cohesive zone laws are used to model the interfacial behavior in the normal and in the tangential directions. In order to keep a level of simplicity amenable to the obtainment of an analytical solution, the two laws are taken as independent. However, a mixed-mode fracture criterion is introduced to couple them in the instant of debonding. Hence, the adopted approach corresponds to the a1 outlined above. The choice of independent cohesive zone laws is also motivated by the lack of any experimental basis for the adoption of a given coupled law for the main application under consideration (namely, bond of FRP to concrete or masonry substrates).

The choice of independent cohesive zone laws enables the use of different values for the mode-I and mode-II interfacial fracture energies, in agreement with the experimental evidence. Tension relates the relative normal displacement, $g_N > 0$, and the normal stress, p_N, while shear relates the relative tangential displacement, g_T, and the tangential stress, p_T. The cohesive laws implemented herein are bilinear (Figure 3). The bilinear shape is simple but able to capture the three characteristic parameters of the interface, i.e. the fracture energies (areas underneath the curves), the cohesive strengths, $p_{N\max}$ and $p_{T\max}$, and the linear elastic properties (slopes of the curves in the ascending branch). For this reason the bilinear model is often used to model the interfacial behaviour of FRP bonded to quasi-brittle substrates (Yuan et al. 2004).

The cohesive laws shown in Figure 3 give the following relationships between the interfacial stresses p_T, p_N and the corresponding relative displacements g_T, g_N

$$\begin{cases} p_T = \dfrac{p_{T\,max}}{g_{T\,max}} g_T & \text{for} \quad 0 \le g_T \le g_{T\,max} \\ p_T = \dfrac{p_{T\,max}}{g_{Tu} - g_{T\,max}} \left(g_{Tu} - g_T \right) & \text{for} \quad g_{T\,max} \le g_T \le g_{Tu} \end{cases} \tag{1}$$

$$\begin{cases} p_N = \dfrac{p_{N\,max}}{g_{N\,max}} g_N & \text{for} \quad 0 \le g_N \le g_{N\,max} \\ p_N = \dfrac{p_{N\,max}}{g_{Nu} - g_{N\,max}} \left(g_{Nu} - g_N \right) & \text{for} \quad g_{N\,max} \le g_N \le g_{Nu} \end{cases} \tag{2}$$

The following ratios are also defined for convenience

$$k_T = \frac{p_{T\max}}{g_{T\max}} \qquad k_N = \frac{p_{N\max}}{g_{N\max}} \qquad \mu_T = \frac{g_{Tu}}{g_{T\max}} \qquad \mu_N = \frac{g_{Nu}}{g_{N\max}} \tag{3}$$

The first two ratios in Eq. (3) represent, respectively, the slopes of the initial (elastic) portions of the cohesive laws in the tangential and normal directions. With the above definitions, the cohesive laws in Eqs. (1) and (2) can be rewritten as follows

$$\begin{cases} p_T = k_T g_T & \text{for} \quad 0 \le g_T \le g_{T\max} \\ p_T = \dfrac{k_T}{\mu_T - 1} \left(g_{Tu} - g_T \right) & \text{for} \quad g_{T\max} \le g_T \le g_{Tu} \end{cases} \tag{4}$$

$$\begin{cases} p_N = k_N g_N & \text{for} \quad 0 \le g_N \le g_{N\max} \\ p_N = \dfrac{k_N}{\mu_N - 1} \left(g_{Nu} - g_N \right) & \text{for} \quad g_{N\max} \le g_N \le g_{Nu} \end{cases} \tag{5}$$

This model adopts a linear mixed-mode failure criterion, as follows

$$\frac{G_I}{G_{If}} + \frac{G_{II}}{G_{IIf}} = 1 \tag{6}$$

where the energy release rates in mode I and mode II, G_I and G_{II}, are identified as the areas under the respective cohesive laws integrated up to the current values of g_N and g_T, and G_{If} and G_{IIf} denote, respectively, the fracture energies in pure mode-I and mode-II conditions. These are given by the total areas underneath the respective cohesive zone laws, hence

$$G_{If} = \frac{1}{2} p_{N\max} g_{Nu} \qquad G_{IIf} = \frac{1}{2} p_{T\max} g_{Tu} \tag{7}$$

The linear criterion is simple but effective, as shown by Kafkalidis and Thouless (2002) and Li et al. (2006), among others. Moreover, it is obviously the most conservative choice for a convex mixed-mode failure criterion.

2.3. Governing equations

Equilibrium of forces of the differential element of the plate (see Figure 2b) along the tangential and the normal directions yields the following equations

$$p_T = t \frac{d\sigma_\theta}{ds} \qquad p_N = \frac{t}{r} \sigma_\theta \tag{8}$$

Equilibrium of moments does not need to be enforced, as it is automatically satisfied. Note that the radial coordinate of the interface has been replaced by the radius of curvature of the centerline of the plate, due to its small thickness. The combination of Eqs. (8) yields

$$p_T = r\frac{dp_N}{ds} \tag{9}$$

Eq. (9) indicates that, for $p_T > 0$, equilibrium dictates that the interfacial normal stress, p_N, has to increase with s, i.e. towards the loaded end of the joint. As will be detailed later, this simple condition has an important consequence in the selection of the possible stages for the status of the interface prior to the onset of debonding.

The linearly elastic behavior of the plate material yields

$$\sigma_\theta = E\varepsilon_\theta \tag{10}$$

where ε_θ is the circumferential strain of the plate. Combining Eqs. (8) and (10) results in

$$p_T = Et\frac{d\varepsilon_\theta}{ds} \qquad p_N = \frac{Et}{r}\varepsilon_\theta \tag{11}$$

The interfacial relative displacements in the tangential and normal directions, g_T and g_N, are defined as

$$g_T = u_\theta - u_{\theta,s} = u_\theta \qquad g_N = u_r - u_{r,s} = u_r \tag{12}$$

where u_θ and $u_{\theta,s}$ are the circumferential displacements of the bottom fiber of the plate and of the top fiber of the substrate, respectively, and u_r and $u_{r,s}$ are the radial displacements of the same fibers. The second equalities of Eqs. (12) stem from the assumption of rigid substrate. This assumption is commonly applied for the analysis of FRP bonded to concrete, where it is widely accepted that the substrate deformations are very low compared with the deformations taking place at the interface. Finally, the following compatibility equation can be written for the plate

$$\varepsilon_\theta = \frac{du_\theta}{ds} + \frac{u_r}{r} \tag{13}$$

Note that u_θ and u_r have been assumed uniform across the plate thickness.

3. ANALYSIS OF THE INTERFACIAL BEHAVIOR PRIOR TO DEBONDING

This section analyzes the distributions of the interfacial stresses prior to the initiation of debonding. In the *a priori* selection of the possible stages, illustrated in Figure 4, it is assumed that the bond length, L, is sufficiently long to guarantee that a portion of the joint close to the free end always remains at the elastic stage in both the tangential and the normal directions. For this assumption to hold, the bond length has to be larger than the effective

bond length, which will be introduced later. The assumption of a "sufficiently long" bond length will be maintained throughout this paper.

At each stage, the interface is subdivided into regions, based on the interfacial behavior in the tangential and in the normal directions. Each region is labeled with two letters, with the first and the second indicating the status of the interface respectively in the tangential and in the normal direction. "E" stands for elastic, and "S" stands for softening. E.g., a region labeled as "SE" is one where the interfacial shear stresses are within the softening branch of the mode-II cohesive law, and the interfacial normal stresses are within the linear-elastic branch of the mode-I cohesive law.

As will be better detailed later, some of the stages depicted in Figure 4 are not compatible with the equilibrium conditions prior to debonding, hence they are not possible. In particular, the feasible stages, which will be analyzed in the following, are only the first two, denoted as EE and EE-SE (Figure 4a,b).

3.1. EE stage

At small loads, the whole length of the interface is at the elastic stage in both the tangential and the normal directions, and no softening or debonding occur (Figure 4a).

Combining Eqs. (4a) and (5a) with Eqs. (11) and (12) yields

$$\begin{cases} k_T u_\theta = Et \dfrac{d\varepsilon_\theta}{ds} \\ k_N u_r = \dfrac{Et}{r} \varepsilon_\theta \end{cases} \tag{14}$$

By using Eq. (13) the following relationships are obtained

$$\begin{cases} k_T u_\theta = Et \left[\dfrac{d^2 u_\theta}{ds^2} + \dfrac{1}{r} \dfrac{du_r}{ds} \right] \\ k_N u_r = \dfrac{Et}{r} \left[\dfrac{du_\theta}{ds} + \dfrac{u_r}{r} \right] \end{cases} \tag{15}$$

Simple manipulation of Eq. (15b) yields

$$u_r = \frac{Etr}{k_N r^2 - Et} \cdot \frac{du_\theta}{ds} \tag{16}$$

Finally, if the first derivative of Eq. (16) is substituted into Eq. (15a), the following differential equation is obtained

$$\frac{d^2 u_\theta}{ds^2} - \lambda^2 \left(1 - \frac{Et}{k_N r^2} \right) u_\theta = 0 \tag{17}$$

where λ has the same definition introduced by Yuan et al. (2004), i.e.

$$\lambda^2 = \frac{k_T}{Et} \tag{18}$$

It can be shown that typical values of the material, geometrical and cohesive law parameters give $Et < k_N r^2$ for the application under examination (see also the examples section). This assumption will be maintained throughout this paper. Therefore Eq. (17) can be rewritten as follows

$$\frac{d^2 u_\theta}{ds^2} - \lambda_r^2 u_\theta = 0 \tag{19}$$

where

$$\lambda_r^2 = \frac{k_T}{Et}\left(1 - \frac{Et}{k_N r^2}\right) = \lambda^2\left(1 - \frac{Et}{k_N r^2}\right) \tag{20}$$

Note that, for $r \to \infty$, $\lambda_r \to \lambda$ and Eq. (19) reduces to the same differential equation for the interfacial shear relative displacement found by Yuan et al. (2004) for the case of a flat substrate. Hence the proposed model is a general one, which reduces to the model valid for bond to flat substrates as a limit case.

The solution of Eq. (19) and the substitution into Eq. (16) yield, respectively

$$\begin{cases} u_{\theta,EE} = A_1 \sinh(\lambda_r s) + A_2 \cosh(\lambda_r s) \\ u_{r,EE} = \dfrac{Etr}{k_N r^2 - Et}\lambda_r \left[A_1 \cosh(\lambda_r s) + A_2 \sinh(\lambda_r s)\right] \end{cases} \tag{21}$$

where the subscript "EE" has been used to refer to the condition where the interfacial stresses are both at the elastic stage, and A_1 and A_2 are two constants that have to be determined. Finally, $\varepsilon_{\theta,EE}$ is readily obtained by substituting $u_{r,EE}$ into Eq. (14b)

$$\varepsilon_{\theta,EE} = \frac{k_N r^2}{k_N r^2 - Et}\lambda_r \left[A_1 \cosh(\lambda_r s) + A_2 \sinh(\lambda_r s)\right] = \frac{\lambda^2}{\lambda_r}\left[A_1 \cosh(\lambda_r s) + A_2 \sinh(\lambda_r s)\right] \tag{22}$$

In the second equality of Eq. (22), the result of Eq. (20) has been introduced. Eqs. (21) and (22) are all valid for $0 \le s \le L$. The unknown constants A_1 and A_2 are easily found imposing two boundary conditions which express equilibrium at the ends

$$\begin{cases} \varepsilon_{\theta,EE}(0) = 0 \\ \varepsilon_{\theta,EE}(L) = \dfrac{F}{Et} \end{cases} \tag{23}$$

Using Eq. (22), the above conditions yield the following values for the constants

$$\begin{cases} A_1 = 0 \\ A_2 = \dfrac{F\lambda_r}{k_T \sinh(\lambda_r L)} \end{cases} \tag{24}$$

Substituting Eqs. (24) into Eqs. (21), the following final results are then obtained for the displacements

$$\begin{cases} u_{\theta,EE} = \dfrac{F\lambda_r}{k_T \sinh(\lambda_r L)} \cosh(\lambda_r s) \\ u_{r,EE} = \dfrac{F}{k_N r \sinh(\lambda_r L)} \sinh(\lambda_r s) \end{cases} \tag{25}$$

Therefore, from Eqs. (4a) and (5a) and recalling Eq. (12), the interfacial stresses result as follows

$$\begin{cases} p_{T,EE}(s) = \dfrac{F\lambda_r}{\sinh(\lambda_r L)} \cosh(\lambda_r s) \\ p_{N,EE}(s) = \dfrac{F}{r \sinh(\lambda_r L)} \sinh(\lambda_r s) \end{cases} \tag{26}$$

Hence the resulting interfacial stresses correspond to simple hyperbolic functions. Their distributions along the bond length will be shown in the examples section. For $r \to \infty$, Eqs. (26) reduce to the equations that Yuan et al. (2004) have given for the case of a flat substrate. In such a case, the interfacial normal stresses are identically zero.

As both $\sinh(\lambda_r s)$ and $\cosh(\lambda_r s)$ are increasing functions for $s > 0$, Eqs. (26) show that the maximum values of both interfacial stresses are reached at the loaded end of the joint, i.e. for $s = L$.

The relationship between the applied force, F, and the displacement of the plate at the loaded end, $d = u_{\theta,EE}(L)$, can be easily computed from Eq. (25a)

$$F = \frac{k_T}{\lambda_r} \tanh(\lambda_r L) d \tag{27}$$

Eq. (27) represents the linear load-displacement relationship in the elastic stage of loading, which is shown as segment OA in Figure 5a.

Eqs. (26) hold until $p_{T,EE}(L) \le p_{T\,max}$ and $p_{N,EE}(L) \le p_{N\,max}$. The force $F_{el,T}$, for which the interface would enter the softening stage in the tangential direction, while still being at the elastic stage in the normal direction, is easily computed from Eq. (26a) imposing $p_{T,EE}(L) = p_{T\,max}$

$$F_{el,T} = p_{T\,max} \frac{\tanh(\lambda_r L)}{\lambda_r} \tag{28}$$

For an infinite bond length (in practice, for bond lengths longer than the effective bond length, see later sections), Eq. (28) converges to the following value

$$F_{el,T} = \frac{p_{T\,\max}}{\lambda_r} \tag{29}$$

Conversely, the force $F_{el,N}$, for which the interface would enter the softening stage in the normal direction, while still being at the elastic stage in the tangential direction, can be computed from Eq. (26b) imposing $p_{N,EE}(L) = p_{N\,max}$

$$F_{el,N} = p_{N\max} r \tag{30}$$

The interface exits the elastic stage when the applied force equals the smallest of $F_{el,T}$ and $F_{el,N}$. It can be shown that the case $F_{el,T} < F_{el,N}$ is by far the most frequent for the realistic range of geometry, material and cohesive parameters valid for the main application of reference, namely, the strengthening of a masonry arch by means of FRP bonded strips (see also the examples section).

3.2. EE-SE stage

If $F_{el,T} < F_{el,N}$, the softening stage is reached first in the tangential direction. This occurs once the interfacial shear stress reaches $p_{T\max}$ at the loaded end, i.e. for $F = F_{el,T}$. As loading progresses, an increasingly long portion of the interface closest to the plate loaded end enters the softening stage in the tangential direction, while the remaining portion of length $\bar{s}$ remains at the elastic stage (Figure 4b). In the normal direction, the interface stays at the elastic stage along the whole length of the joint. During this phase the load increases as the length of the elastic zone, $\bar{s}$, decreases.

In this case, combining Eqs. (4b) and (5a) with Eqs. (11) and (12) yields

$$\begin{cases} \dfrac{k_T}{\mu_T - 1}\left(g_{Tu} - u_\theta\right) = Et\dfrac{d\varepsilon_\theta}{ds} \\ k_N u_r = \dfrac{Et}{r}\varepsilon_\theta \end{cases} \tag{31}$$

By using Eq. (13) the following relationships are then obtained

$$\begin{cases} \dfrac{k_T}{\mu_T - 1}\left(g_{Tu} - u_\theta\right) = Et\left[\dfrac{d^2 u_\theta}{ds^2} + \dfrac{1}{r}\dfrac{du_r}{ds}\right] \\ k_N u_r = \dfrac{Et}{r}\left[\dfrac{du_\theta}{ds} + \dfrac{u_r}{r}\right] \end{cases} \tag{32}$$

Eq. (32b) is obviously identical to Eq. (15b), hence Eq. (16) continues to hold. If the first derivative of Eq. (16) is substituted into Eq. (32a), the following differential equation is obtained

$$\frac{d^2 u_\theta}{ds^2} + \lambda_{rs,T}^2 u_\theta = \lambda_{rs,T}^2 g_{Tu} \tag{33}$$

where

$$\lambda_{rs,T}^2 = \frac{\lambda_r^2}{\mu_T - 1} \tag{34}$$

Eq. (33) replaces Eq. (19) in the interfacial region where tangential softening takes place. The solution of Eq. (33) and the substitution into Eq. (16) yield

$$\begin{cases} u_{\theta,SE} = g_{Tu} + B_1\, sin(\lambda_{rs,T} s) + B_2\, cos(\lambda_{rs,T} s) \\ u_{r,SE} = \dfrac{Etr}{k_N r^2 - Et} \lambda_{rs,T} \left[B_1\, cos(\lambda_{rs,T} s) - B_2\, sin(\lambda_{rs,T} s) \right] \end{cases} \quad \text{for} \quad \bar{s} \le s \le L \tag{35}$$

where the subscript "SE" has been added to refer to the portion of the joint where the interfacial tangential and normal stresses are respectively within the softening and elastic branches of the respective cohesive laws (Figure 4b). Finally, $\varepsilon_{\theta,SE}$ is readily obtained from the substitution of $u_{r,SE}$ into Eq. (31b)

$$\varepsilon_{\theta,SE} = \frac{k_N r^2}{k_N r^2 - Et} \lambda_{rs,T} \left[B_1\, cos(\lambda_{rs,T} s) - B_2\, sin(\lambda_{rs,T} s) \right] = \frac{\lambda^2}{\lambda_r^2} \lambda_{rs,T} \left[B_1\, cos(\lambda_{rs,T} s) - B_2\, sin(\lambda_{rs,T} s) \right] \tag{36}$$

Again, the above equation is valid for $\bar{s} \le s \le L$. In the elastic region, Eqs. (21) and (22) continue to hold but with dfferent values of the constants, hence

$$\begin{cases} u_{\theta,EE} = C_1\, sinh(\lambda_r s) + C_2\, cosh(\lambda_r s) \\ u_{r,EE} = \dfrac{Etr}{k_N r^2 - Et} \lambda_r \left[C_1\, cosh(\lambda_r s) + C_2\, sinh(\lambda_r s) \right] \\ \varepsilon_{\theta,EE} = \dfrac{\lambda^2}{\lambda_r} \left[C_1\, cosh(\lambda_r s) + C_2\, sinh(\lambda_r s) \right] \end{cases} \tag{37}$$

Eqs. (37) are all valid for $0 \le s \le \bar{s}$. The four unknown constants B_1, B_2, C_1 and C_2, plus the length of the elastic zone, $\bar{s}$, are found imposing the following five boundary conditions

$$\begin{cases} \varepsilon_{\theta,EE}(0) = 0 \\ u_{\theta,EE}(\bar{s}) = g_{T\,max} \\ u_{\theta,SE}(\bar{s}) = g_{T\,max} \\ \varepsilon_{\theta,EE}(\bar{s}) = \varepsilon_{\theta,SE}(\bar{s}) \\ \varepsilon_{\theta,SE}(L) = \dfrac{F}{Et} \end{cases} \tag{38}$$

By using the first four conditions, the following expressions of the unknown constants as functions of $\bar{s}$ are obtained

$$\begin{cases} C_1 = 0 \\ C_2 = \dfrac{g_{T\max}}{\cosh\left(\lambda_r \bar{s}\right)} \\ B_1 = -\sin\left(\lambda_{rs,T}\bar{s}\right)\left(g_{Tu} - g_{T\max}\right) + \cos\left(\lambda_{rs,T}\bar{s}\right)\sqrt{\mu_T - 1}\cdot g_{T\max}\tanh\left(\lambda_r \bar{s}\right) \\ B_2 = -\cos\left(\lambda_{rs,T}\bar{s}\right)\left(g_{Tu} - g_{T\max}\right) - \sin\left(\lambda_{rs,T}\bar{s}\right)\sqrt{\mu_T - 1}\cdot g_{T\max}\tanh\left(\lambda_r \bar{s}\right) \end{cases} \tag{39}$$

Substituting these constants into Eqs. (37a,b) and (35), by straightforward manipulations, yields the following expressions for the displacements as functions of $\bar{s}$ in the EE and SE regions, respectively

$$\begin{cases} u_{\theta,EE} = \dfrac{g_{T\max}}{\cosh\left(\lambda_r \bar{s}\right)}\cosh\left(\lambda_r s\right) \\ u_{r,EE} = \dfrac{p_{T\max}}{k_N \lambda_r r \cosh\left(\lambda_r \bar{s}\right)}\sinh\left(\lambda_r s\right) \end{cases} \quad \text{for } 0 \le s \le \bar{s} \tag{40}$$

$$\begin{cases} u_{\theta,SE} = \left(g_{Tu} - g_{T\max}\right)\left\{\dfrac{g_{Tu}}{g_{Tu} - g_{T\max}} - \cos\left[\lambda_{rs,T}\left(s - \bar{s}\right)\right] + \dfrac{\lambda_{rs,T}}{\lambda_r}\tanh\left(\lambda_r \bar{s}\right)\sin\left[\lambda_{rs,T}\left(s - \bar{s}\right)\right]\right\} \\ u_{r,SE} = \dfrac{p_{T\max}}{\lambda_{rs,T} k_N r}\left\{\sin\left[\lambda_{rs,T}\left(s - \bar{s}\right)\right] + \dfrac{\lambda_{rs,T}}{\lambda_r}\tanh\left(\lambda_r \bar{s}\right)\cos\left[\lambda_{rs,T}\left(s - \bar{s}\right)\right]\right\} \end{cases} \quad \text{for } \bar{s} \le s \le L \tag{41}$$

Therefore the interfacial stresses as functions of $\bar{s}$ result as follows

$$\begin{cases} p_{T,EE} = \dfrac{p_{T\max}}{\cosh\left(\lambda_r \bar{s}\right)}\cosh\left(\lambda_r s\right) \\ p_{N,EE} = \dfrac{p_{T\max}}{\lambda_r r \cosh\left(\lambda_r \bar{s}\right)}\sinh\left(\lambda_r s\right) \end{cases} \quad \text{for } 0 \le s \le \bar{s} \tag{42}$$

$$\begin{cases} p_{T,SE} = p_{T\max}\left\{\cos\left[\lambda_{rs,T}\left(s - \bar{s}\right)\right] - \dfrac{\lambda_{rs,T}}{\lambda_r}\tanh\left(\lambda_r \bar{s}\right)\sin\left[\lambda_{rs,T}\left(s - \bar{s}\right)\right]\right\} \\ p_{N,SE} = \dfrac{p_{T\max}}{\lambda_{rs,T} r}\left\{\sin\left[\lambda_{rs,T}\left(s - \bar{s}\right)\right] + \dfrac{\lambda_{rs,T}}{\lambda_r}\tanh\left(\lambda_r \bar{s}\right)\cos\left[\lambda_{rs,T}\left(s - \bar{s}\right)\right]\right\} \end{cases} \quad \text{for } \bar{s} \le s \le L \tag{43}$$

Moreover, the substitution of Eqs. (39c,d) into Eq. (36) yields

$$\varepsilon_{\theta,SE} = \frac{p_{T\,max}}{Et\lambda_{rs,T}}\left\{sin\left[\lambda_{rs,T}\left(s - \bar{s}\right)\right] + \frac{\lambda_{rs,T}}{\lambda_r}tanh\left(\lambda_r \bar{s}\right)cos\left[\lambda_{rs,T}\left(s - \bar{s}\right)\right]\right\} \tag{44}$$

Finally, Eq. (44) combined with the fifth boundary condition in Eq. (38) gives the relationship between the applied force and $\bar{s}$

$$F = \frac{p_{T\,max}}{\lambda_{rs,T}}\left\{sin\left[\lambda_{rs,T}\left(L - \bar{s}\right)\right] + \frac{\lambda_{rs,T}}{\lambda_r}tanh\left(\lambda_r \bar{s}\right)cos\left[\lambda_{rs,T}\left(L - \bar{s}\right)\right]\right\} \tag{45}$$

from which, for each value of $\bar{s}$, the corresponding value of F can be computed. The displacement of the plate at the loaded end during this stage, $d = u_{\theta,SE}(L)$, can be easily computed from Eq. (41a)

$$d = (g_{Tu} - g_{T\,max})\left\{\frac{g_{Tu}}{g_{Tu} - g_{T\,max}} - cos\left[\lambda_{rs,T}\left(L - \bar{s}\right)\right] + \frac{\lambda_{rs,T}}{\lambda_r} tanh\left(\lambda_r \bar{s}\right) sin\left[\lambda_{rs,T}\left(L - \bar{s}\right)\right]\right\} \quad (46)$$

The combination of Eqs. (45) and (46) yields the non-linear load-displacement relationship in the EE-SE stage of loading, which is denoted by AB in Figure 5a.

3.3. Analysis of the interfacial behavior during the EE and EE-SE stages

The progressive configuration of the interfacial stresses during the EE and EE-SE stages can be easily followed using the relationships derived earlier. The main steps are outlined herein:

- during the EE stage, the interfacial stresses are given by Eqs. (26) along the entire length of the joint. Such stresses are directly proportional to the applied load. Hence, during this stage, the behavior of the interface can be followed by gradually increasing the value of F. Assuming $F_{el,T} < F_{el,N}$, this stage ends when the applied load reaches the value $F_{el,T}$, given by Eq. (28);

- during the EE-SE stage, the behavior of the interface can be followed by gradually decreasing the length of the elastic region, $\bar{s}$. At the beginning of this stage, it is obviously $\bar{s} = L$. For each value of $\bar{s}$, the corresponding value of the applied force can be computed from Eq. (45), and the interfacial stress distributions are obtained from Eqs. (42) and (43).

3.4. EE-ES, EE-SE-SS and EE-ES-SS stages

If $F_{el,N} < F_{el,T}$, the softening stage would be reached first in the normal direction. This would occur once the interfacial normal stress reaches $p_{N\max}$ at the loaded end, i.e. for $F = F_{el,N}$. With the progression of loading, an increasingly long portion of the interface closest to the plate loaded end would be expected to enter the softening stage in the normal direction, with the remaining portion of length $\bar{s}$ still at the elastic stage (EE-ES stage, Figure 4c).

The situation outlined above, apparently dual of the analogous one described for the EE-SE stage, is in fact not compatible with the equilibrium requirements prior to debonding, i.e. with a situation of increasing applied load. Hence it is not a real possible situation prior to debonding. As shown by Eq. (9), equilibrium dictates that for $p_T > 0$ it is $\frac{dp_N}{ds} > 0$, i.e. the interfacial normal stress has to increase towards the loaded end of the joint. Conversely, in presence of a softening zone in the normal direction ($\bar{s} \le s \le L$, Figure 4c), the interfacial normal stress would equal $p_{N\,max}$ for $s = \bar{s}$ and would have to decrease towards the loaded end.

For the same reason, stages EE-ES-SS and EE-SE-SS are also not possible prior to debonding. More in general, stages where interfacial softening occurs in the normal direction are not compatible with the equilibrium requirements for an increasing external load and hence are not feasible prior to debonding.

The above considerations permit to conclude that, for $F_{el,N} < F_{el,T}$, an applied force value $F = F_{el,N}$ results directly into debonding. The same conclusion can also be drawn from Eq. (8b) written for $s = L$, i.e. at the plate loaded end

$$p_N(L) = \frac{t}{r}\sigma_\theta(L) = \frac{F}{r} \tag{47}$$

From Eq. (47) it is evident that the maximum value of force applicable to the joint cannot be larger than $F_{el,N}$ as given by Eq. (30).

4. COMPUTATION OF THE DEBONDING LOAD AND OF THE EFFECTIVE BOND LENGTH

4.1. Possible paths to debonding

As a consequence of what illustrated in the previous sections, the joint may follow three alternative paths to debonding:

a. if $F_{el,T} < F_{el,N}$, the EE stage evolves into the EE-SE stage. In this case, two subcases are possible:
   - a1. The debonding condition is reached during the EE-SE stage (see Section 4.2), provided that the corresponding load $F_{deb} < F_{el,N}$. In summary, in this case it is $F_{el,T} < F_{deb} < F_{el,N}$, where F_{deb} is the debonding load (Figure 5a). Debonding is triggered by the combination of the interfacial tangential and normal stresses, according to the mixed-mode fracture criterion in Eq. (6);
   - a2. If $F_{el,N}$ is attained at any point during the EE-SE stage, the debonding condition is reached and $F_{deb} = F_{el,N}$. In summary, in this case it is $F_{el,T} < F_{deb} = F_{el,N}$ (Figure 5b). Debonding is triggered by the interfacial normal stresses;

b. if $F_{el,N} < F_{el,T}$, the debonding condition is reached directly at the end of the EE stage, and $F_{deb} = F_{el,N}$. In summary, in this case it is $F_{deb} = F_{el,N} < F_{el,T}$ (Figure 5c). Debonding is triggered by the interfacial normal stresses.

More details will be reported in the examples section. It is worth noting that the limit case of a flat surface falls within subcase a1, being $F_{el,N} \to \infty$ for $r \to \infty$.

Once debonding is initiated, the proposed model can no longer follow the behavior of the joint. In fact, assuming that the applied force maintains the initial direction during debonding, the presence of bending and shear forces can no longer be neglected.

4.2. Computation of the debonding load and of the effective bond length at debonding for case a1

In case a1, where debonding is initiated by the combination of interfacial tangential and normal stresses, the debonding load, F_{deb}, is reached during the EE-SE stage.

If no mixed-mode failure criterion were introduced, debonding would occur at the end of the EE-SE stage, as shown in the following. F would reach its maximum value when the derivative of Eq. (45) with respect to $\bar{s}$ equals zero. Therefore, the value of $\bar{s}$ at debonding, $\bar{s}_{deb,\max}$, would be found from the following relationship

$$\tanh\left(\lambda_r \bar{s}_{deb\max}\right) = \frac{\lambda_{rs,T}}{\lambda_r}\tan\left[\lambda_{rs,T}\left(L-\bar{s}_{deb\max}\right)\right] \tag{48}$$

The substitution of Eq. (48) into Eq. (45) would yield

$$F_{deb,\max} = \frac{p_{T\max}}{\lambda_{rs,T}}\frac{g_{Tu}}{g_{Tu}-g_{T\max}}\sin\left[\lambda_{rs,T}\left(L-\bar{s}_{deb,\max}\right)\right] \tag{49}$$

where $F_{deb,\max}$ has been used to denote the debonding load which would be obtained in case a1 if no mixed-mode failure criterion were introduced. This is an upper bound to the actual debonding load.

Note that the above relationships are analogous to those found by Yuan et al. (2004) for the case of a flat substrate, with the exception of the dependence on the radius of curvature included into λ_r and $\lambda_{rs,T}$. The same authors also noted that, for infinite bond lengths (in practice, for bond lengths longer than the effective bond length), the debonding load is reached when $p_T = 0$ (or, equivalently, when $g_T = g_{Tu}$) at the loaded end of the plate. Given the strict analogy in the equations, the same condition would hold for curved substrates, assuming that no mixed-mode effects were taken into account. Hence, debonding would occur at the end of the EE-SE stage.

When a mixed-mode failure criterion is introduced, debonding occurs before the end of the EE-SE stage, hence the debonding load, F_{deb}, is less than $F_{deb,\max}$. Also, it is $p_T > 0$ and $g_T < g_{Tu}$ at the plate loaded end, unlike in the case of a flat substrate.

In order to enforce the mixed-mode failure criterion, the energy release rates G_I and G_{II} need to be computed. Recalling Eq. (12), the interfacial relative displacements in the tangential and normal directions are equal to u_θ and u_r, respectively. From Eqs. (40) and (41) it can be shown that these are maximum at the loaded end of the joint, and these maximum values are given by Eqs. (41)

$$\begin{cases} g_T(L) = u_{\theta,SE}(L) = \left(g_{Tu}-g_{T\max}\right)\left\{\dfrac{g_{Tu}}{g_{Tu}-g_{T\max}} - \cos\left[\lambda_{rs,T}\left(L-\bar{s}\right)\right] + \dfrac{\lambda_{rs,T}}{\lambda_r}\tanh\left(\lambda_r\bar{s}\right)\sin\left[\lambda_{rs,T}\left(L-\bar{s}\right)\right]\right\} \\ g_N(L) = u_{r,SE}(L) = \dfrac{p_{T\max}}{\lambda_{rs,T}k_N r}\left\{\sin\left[\lambda_{rs,T}\left(L-\bar{s}\right)\right] + \dfrac{\lambda_{rs,T}}{\lambda_r}\tanh\left(\lambda_r\bar{s}\right)\cos\left[\lambda_{rs,T}\left(L-\bar{s}\right)\right]\right\} \end{cases} \tag{50}$$

The corresponding values of the interfacial stresses are readily obtained from Eqs. (43)

$$\begin{cases} p_{T,SE}(L) = p_{T\max}\left\{\cos\left[\lambda_{rs,T}\left(L-\bar{s}\right)\right] - \dfrac{\lambda_{rs,T}}{\lambda_r}\tanh\left(\lambda_r\bar{s}\right)\sin\left[\lambda_{rs,T}\left(L-\bar{s}\right)\right]\right\} \\ p_{N,SE}(L) = \dfrac{p_{T\max}}{\lambda_{rs,T}r}\left\{\sin\left[\lambda_{rs,T}\left(L-\bar{s}\right)\right] + \dfrac{\lambda_{rs,T}}{\lambda_r}\tanh\left(\lambda_r\bar{s}\right)\cos\left[\lambda_{rs,T}\left(L-\bar{s}\right)\right]\right\} \end{cases} \tag{51}$$

Note that all the interfacial relative displacements and stresses given above are functions of the length of the elastic region of the joint, $\bar{s}$.

The maximum values of the mode-I and mode-II energy release rates during the EE-SE stage are then reached at the loaded end of the joint, and can be computed as the areas underneath the respective cohesize zone laws (Figure 6)

$$\begin{cases} G_I(L) = \dfrac{1}{2} g_N(L) p_{N,SE}(L) = \dfrac{1}{2} k_N g_N^2(L) \\ G_{II}(L) = G_{IIf} - \dfrac{1}{2} p_{T,SE}(L)\left[g_{Tu} - g_T(L)\right] \end{cases} \tag{52}$$

recalling that the interface is in elastic conditions in the normal direction and in elastic-softening conditions in the tangential direction. Due to the earlier results, also the energy release rates will be a function of $\bar{s}$.

As illustrated in Section 3.3, during the EE-SE stage the behavior of the interface is followed by gradually decreasing the length of the elastic portion $\bar{s}$. As $\bar{s}$ decreases, $g_T(L)$ and $g_N(L)$ both increase, and the energy release rates in Eq. (52) increase correspondingly (see also Figure 6). For a certain value of this length, $\bar{s}_{deb}$, these energy release rates will satisfy the mixed-mode failure criterion in Eq. (6). The load corresponding to this value of $\bar{s}$ through Eq. (45) is the debonding load.

At debonding, only a limited portion of the interface is subjected to significant interfacial stresses, and the length of this portion is generally termed "effective bond length" (De Lorenzis et al. 2001, Yuan et al. 2004). Yuan et al. (2004) defined the effective bond length at debonding, $L_{eff,deb}$, as the bond length for which the debonding load is equal to 97% of that corresponding to a joint with an infinite bond length. The expression of $L_{eff,deb}$ can be taken directly from Yuan et al. (2004) as follows

$$L_{eff,deb} = a + \frac{1}{2\lambda_r} \ln \frac{\lambda_r + \lambda_{rs,T} \tan\left(\lambda_{rs,T} a\right)}{\lambda_r - \lambda_{rs,T} \tan\left(\lambda_{rs,T} a\right)} \tag{53}$$

where

$$a = \frac{1}{\lambda_{rs,T}} \arcsin\left[0.97 \sqrt{\frac{g_{Tu} - g_{T\max}}{g_{Tu}}} \right] \tag{54}$$

For cases a2 and b, the debonding load is equal to $F_{deb} = F_{el,N}$. In these cases, the above definition of the effective bond length at debonding looses significance, as the debonding load does no longer depend on the bond length. An alternative definition could be introduced if desired. This aspect deserves further investigation.

5. NUMERICAL MODELING

In the numerical finite element model, the cohesive laws in Eqs. (1) and (2) have been implemented into a contact element based on the node-to-segment strategy as employed in Wriggers et al. (1998), and generalized to handle cohesive forces in both the normal and tangential directions. In the normal direction under compression the non-penetration condition is enforced using the penalty method. Depending on the contact status, an automatic

switching procedure is used to choose between cohesive and contact models. Each element contribution for the cohesive and contact forces is suitably added to the global virtual work equation as

$$\delta W_c = F_N \delta g_N + F_T \delta g_T \tag{55}$$

where δW_c is the contact contribution to the virtual work, and F_N and F_T denote, respectively, the normal and tangential contact force.

Figure 7 shows two representative discretized geometries. The adherend is modeled with two-dimensional, finite deformation, linearly-elastic beam elements, whereas the substrate is discretized with 4-node isoparametric plane stress elastic elements. The substrate elements are characterized by a very large elastic modulus, in order to minimize the effects of the substrate compliance on results. The non-linear problem is solved with a Newton-Raphson procedure, where the global tangent stiffness matrix is properly obtained with a consistent linearization of all the contributions given by Eq. (55). Such linearization yields (Paggi 2005)

$$\Delta\delta W_c = \left(\frac{\partial F_N}{\partial g_N}\Delta g_N + \frac{\partial F_N}{\partial g_T}\Delta g_T\right)\delta g_N + \left(\frac{\partial F_T}{\partial g_T}\Delta g_N + \frac{\partial F_T}{\partial g_T}\Delta g_T\right)\delta g_T + F_N \Delta\delta g_N + F_T \Delta\delta g_T \tag{56}$$

where the symbols δ and Δ denote, respectively, virtual variation and linearization. The geometrical parameters δg_N, δg_T (with their symmetric ones Δg_N, Δg_T), $\Delta\delta g_N$ and $\Delta\delta g_T$ are easily determined based on the contact element geometry (Zavarise 1991, Paggi 2005). The partial derivatives of the normal and tangential forces with respect to both normal and tangential relative displacements depend on the cohesive law parameters. For the laws chosen in this study, it is (see also Figure 3)

$$\frac{\partial F_N}{\partial g_N} = \begin{cases} \varepsilon_N A & \text{for} \quad g_N < 0 \\ \dfrac{p_{N\max}}{g_{N\max}} A & \text{for} \quad 0 \le g_N < g_{N\max} \\ -\dfrac{p_{N\max}}{g_{Nu} - g_{N\max}} A & \text{for} \quad g_{N\max} \le g_N < g_{Nu} \end{cases} \tag{57}$$

$$\frac{\partial F_T}{\partial g_T} = \begin{cases} \dfrac{p_{T\max}}{g_{T\max}} A & \text{for} \quad |g_T| < g_{T\max} \\ -\dfrac{p_{T\max}}{g_{Tu} - g_{T\max}} A & \text{for} \quad g_{T\max} \le |g_T| < g_{Tu} \end{cases} \tag{58}$$

Moreover, due to the uncoupled formulation, it is

$$\frac{\partial F_N}{\partial g_T} = \frac{\partial F_T}{\partial g_N} = 0 \tag{59}$$

where ε_N is the penalty parameter, and A is the contact area associated to each contact element.

Also in the numerical model, the energy release rates in mode I and mode II are identified for each contact element as the areas under the respective cohesive laws integrated up to the current values of g_N and g_T for the element, and the mixed-mode failure criterion in Eq. (6) is assumed. Once the failure criterion is met for an element in the cohesive zone, the element is assumed to be no longer capable to bear any load.

The discretization is refined appropriately to yield mesh-independent results. The model is implemented in the finite element code FEAP (courtesy of Prof. R.L. Taylor).

6. EXAMPLES

6.1. Example 1 (case a1, $F_{el,T} < F_{deb} < F_{el,N}$)

In the first example, the chosen input values are realistic for FRP sheets bonded to a concrete or masonry substrate, see e.g. Chen and Teng (2001), CNR DT200/2004, and Dai et al. (2004). The values thus adopted for the parameters involved in the problem are reported in Table 1. The curvature radius is given the values 200 mm, 500 mm, and infinite (flat substrate). The bond length is chosen as $L = 150$ mm, i.e. longer than the effective bond length given by Eq. (53). With reference to Eq. (17) and to the related comments, it may be noticed that the inequality $Et < k_N r^2$ is largely satisfied, hence the equations presented in the paper are applicable. The values of $F_{el,T}$, $F_{el,N}$ and F_{deb} are reported in Table 2. The value of $F_{deb\max}$ is also reported for comparison.

Figures 8 and 9 illustrate the results, respectively, for the EE and for the EE-SE stages. The curves clearly show that the substrate curvature has no appreciable effect on the magnitude and distribution of the interfacial shear stresses. This applies to both the EE and the EE-SE stages. Conversely, a significant influence is visible on the interfacial normal stresses. These are identically zero in the case of a flat substrate, and their magnitude increases as the substrate curvature radius decreases. As expected, tensile normal stresses are obtained as a result of the concave shape of the substrate. An excellent agreement is found between analytical and numerical results, the respective curves being virtually coincident.

Figure 10 illustrates the interfacial stress distributions at the onset of debonding. In the case of a flat substrate, the interfacial shear stress at debonding reaches zero at the loaded end, which implies that the entire EE-SE stage has been exploited. This does no longer hold in the case of curved substrates. Due to the presence of the interfacial normal stresses, the onset of debonding is predicted to occur when the combination of the mode-I and mode-II energy release rates at the loaded end reaches the boundary of Eq. (6). As the substrate curvature increases, the interfacial shear stresses undergo negligible variations whereas the normal stresses increase considerably (Figures 8 and 9). Correspondingly, for a given load the value of G_{II} at the loaded end remains unchanged whereas the value of G_I increases. Thus, as the curvature increases the load at onset of debonding decreases and the condition in Eq. (6) is met for a progressively larger value of the interfacial shear stress at the loaded end (Figure 10a).

As visible from the values in Table 2, the reduction of the debonding load due to the curvature for the considered example is rather weak. This is due to the fact that the interfacial normal stresses are considerably smaller than the shear stresses, hence the contribution of the mode-I component to the first member of Eq. (6) is rather small. In general, the extent to which the debonding load is influenced by the substrate curvature in case a1 will be a function of the material, geometry and cohesive parameters valid for the interface under examination.

If no mixed-mode failure criterion were assumed, the debonding load would be equal to $F_{deb,\max}$. This is practically insensitive to the curvature due to the fact that the interfacial shear stresses are practically independent from r.

The comparison of the proposed model predictions with test results would certainly be of interest. Unfortunately, the few bond test results currently available in the literature are not suitable for a comparison with the predictions of the proposed model. In fact, some of these results have been obtained from bending pull-out tests (Aiello et al. 2001, 2004), and this test setup introduces significant spurious normal stresses due to the bending effect. The other results have been obtained from a direct pull-out test setup (Basilio Sanchez 2007) but unfortunately they are insufficiently documented to attempt a comparison. In particular, the radius of curvature of the substrate is not reported. Nevertheless, these latter test results show a reduction of 4% in the debonding load between specimens with flat and concave substrates, and the entity of this reduction is of the same order of magnitude of that shown in Table 1. It is also worth noting that tests showing a dramatic influence of the substrate curvature on the debonding load would likely be affected by an imperfect tangency condition between the plate and the substrate at the loaded end. In fact, previous research (De Lorenzis and Zavarise 2008) demonstrated the high sensitivity of the debonding load to the angle between the applied load and the substrate at the loaded end of the plate.

Figure 11 illustrates the load vs. loaded-end displacement curves. There is no appreciable influence of the substrate curvature on the obtained behavior, up to the debonding load which is moderately influenced by the curvature as mentioned earlier. The two stages in the behavior of the interface are clearly visible, with a linear force-displacement relationship during stage EE followed by a non-linear trend during stage EE-SE. The analytical and numerical curves are virtually coincident, showing an excellent agreement between the two models.

Finally, Table 2 reports the effective bond length at debonding, as computed by the analytical model. Its value shows a weak dependence from the substrate curvature.

6.2. Example 2 (case a2, $F_{el,T} < F_{deb} = F_{el,N}$)

In the second example, the values adopted for the parameters involved in the problem are reported in Table 1. The curvature radius is given the values 150 mm, 200 mm, and 250 mm. The bond length is chosen as $L = 150$ mm. Once again the inequality $Et < k_N r^2$ is largely satisfied, hence the equations presented in the paper are applicable. The values of $F_{el,T}$, $F_{el,N}$ and F_{deb} are reported in Table 3.

Figures 12 and 13 illustrate the results respectively for the EE stage and for the EE-SE stage. The same observations made earlier for example 1 are still applicable in this case. Unlike in the first example, in this case the interfacial stress at the loaded end is significantly larger than zero prior to debonding. This is due to the fact that only part of the EE-SE stage is exploited, as debonding occurs abruptly when the applied force reaches $F_{el,N}$.

Figure 14 illustrates the load vs. loaded-end displacement curves. Once again there is no appreciable influence of the substrate curvature on the obtained behavior. However, the debonding load is now linearly dependent on the radius of curvature, being equal to $F_{el,N}$. The two stages in the behavior of the interface are clearly visible, with a linear force-displacement relationship during stage EE followed by a non-linear trend during stage EE-SE. The analytical and numerical curves are again virtually coincident, showing an excellent agreement between the two models. However, a small discrepancy is observed in the prediction of the debonding load, which is slightly overestimated by the numerical model. This is probably due to the error inherent to the discretization of a curved surface with linear

elements, and to the high sensitivity of the debonding load to very small discrepancies in prediction of the interfacial normal stress at the loaded end.

6.3. Example 3 (case b, $F_{deb} = F_{el,N} < F_{el,T}$)

In the third example, the values adopted for the parameters involved in the problem are the same of example 2 (see also Table 1). The curvature radius is given the values 50 mm, 75 mm, and 100 mm. The bond length is chosen as $L = 75$ mm. The values of $F_{el,T}$, $F_{el,N}$ and F_{deb} are reported in Table 4.

Figure 15 illustrates the results for the EE stage, which is the only stage encountered prior to debonding. Once again the curves clearly show that the substrate curvature has no appreciable effect on the magnitude and distribution of the interfacial shear stresses. Conversely, a significant influence is visible on the interfacial normal stresses. An excellent agreement is found between analytical and numerical results.

Figure 16 illustrates the load vs. loaded-end displacement curves. There is no appreciable influence of the substrate curvature on the obtained behavior, which is linear with slightly different values of slope for the three curvature values. However, as in Example 2 the debonding load is equal to $F_{el,N}$ and thus is linearly dependent on the radius of curvature. The analytical and numerical curves are virtually coincident, showing an excellent agreement between the two models. However, the same discrepancy evidenced for Example 2 is observed here, the numerical debonding load being always slightly larger than the analytical one.

7. CONCLUSIONS

A new analytical model has been developed for the interfacial stresses between a thin plate and a rigid substrate with simple constant curvature. Also, a numerical model where the interface is modeled by zero-thickness node-to-segment contact elements has been devised. The interfacial behavior has been described with bilinear independent cohesive laws in the normal and tangential directions, coupled with a mixed-mode fracture criterion.

The models have been used to determine the interfacial shear and normal stresses as functions of the substrate curvature prior to the initiation of debonding, as well as to estimate the debonding load and the effective bond length of the joint. The evolution of the interface from the initial stage of loading to the onset of debonding has been examined for the three possible cases that have been identified. The following main conclusions can be drawn:

- there are two feasible stages in the behavior of the interface prior to the onset of debonding, whereby the interfacial stresses are both within the elastic branch of the cohesive laws (EE stage), or within the softening branch in the tangential direction and within the elastic one in the normal direction (EE-SE stage);
- stages where the interfacial normal stresses are within the softening branch of the cohesive law do not fulfil equilibrium requirements prior to debonding, and therefore are not feasible;
- three possible paths to the initiation of debonding exist, one in which debonding is triggered by the combination of interfacial tangential and normal stresses, and two in which debonding results from the normal stresses. The path followed by the joint depends on the combination of material, geometry and cohesive parameters. The corresponding debonding load can be evaluated by the proposed analytical model;

- at all stages, the substrate curvature has no appreciable influence on the magnitude and distribution of the interfacial shear stresses, as well as on the load-displacement relationship, whereas it affects significantly the interfacial normal stresses;
- if debonding is triggered by the combination of interfacial tangential and normal stresses, the debonding load is influenced by the substrate curvature to an extent depending on the combination of the different material, geometry and cohesive parameters. If debonding is triggered by the normal stresses, the debonding load depends linearly on the radius of curvature;
- the effective bond length at debonding, defined by previous researchers (Yuan et al. 2004), is weakly influenced by the substrate curvature for the case where debonding is triggered by both the tangential and normal stresses. If debonding is triggered by the normal stresses, the established definition of the effective bond length looses significance, therefore an alternative definition should be introduced;
- the presented analytical and numerical models are effective tools to examine the behavior and capacity of the bonded joint and provide results which are in excellent mutual agreement.

A complete assessment of the influence of the substrate curvature on the bond performance of thin bonded plates needs to account not only for the initiation of debonding, but also for the subsequent behavior during the debonding process. During this process, assuming that the direction of the applied load remains unchanged, the bonded plate is subjected to a "peel test" condition with increasing peel angle. Previous research (De Lorenzis and Zavarise 2008) demonstrated the high sensitivity of the debonding load to the peel angle. Therefore, unlike in the case of a flat substrate, the debonding process is expected to occur under a decreasing load. A fracture mechanics approach analyzing this process will be presented in a forthcoming paper.

8. REFERENCES

Aiello, M. A., Galati, N., La Tegola, A. (2001). "Bond Analysis of Curved Structural Concrete Elements Strengthened using FRP Materials", Proceedings FRPRCS-5, Cambridge, UK.

Aiello, M.A., De Lorenzis, L., Galati, N., La Tegola, A. (2004). "Bond between FRP laminates and curved concrete substrates with anchoring composite spikes", Proceedings IMTCR'04, Lecce, Italy.

Basilio Sanchez, I. (2007). Strengthening of arched masonry structures with composite materials. PhD Thesis, University of Minho, Portugal.

Chen, J.F., Teng, J.G. (2001). "Anchorage strength models for FRP and steel plates bonded to concrete", *Journal of Structural Engineering*, ASCE, 127(7): 784-791.

CNR-DT 200/2004 (2004). "Guide for the Design and Construction of Externally Bonded FRP Systems for Strengthening Existing Structures - Materials, RC and PC structures, masonry structures", CNR, Rome 13 July 2004 (English version).

Dai, J.G., Ueda, T., Sato, Y., Hadiyono, J. (2004). "Dowel resistances of bond interfaces between FRP sheets and concrete". *Proceedings of the Second International Conference on FRP Composites in Civil Engineering*, Adelaide, Australia, 371-379.

De Lorenzis, L. (2008). "Strengthening of masonry structures with FRP composites", Chapter 10 in "Strengthening and Rehabilitation of Structural Members using Advanced Fibre/Polymer Composites", Editors L. Hollaway and J.G. Teng, Woodhead Publishing Ltd, Cambridge, UK, ISBN 1 84569 448 1, 416 pp.

De Lorenzis, L., Dimitri, R., La Tegola, A. (2007). "Reduction of the lateral thrust of masonry arches and vaults with FRP composites", *Construction and Building Materials*, 21(7): 1415-1430.

De Lorenzis, L., Miller, B., Nanni, A. (2001). "Bond of FRP Laminates to Concrete". *ACI Materials Journal*, 98 (3): 256-264.

De Lorenzis, L., Teng, J.G., Zhang, L. (2006). "Elastic interfacial stresses in curved members bonded with a thin plate". *International Journal of Solids and Structures*, 43 (25-26): 7501-7517.

De Lorenzis, L., Zavarise, G. (2008). "Modeling of mixed-mode debonding in the peel test applied to superficial reinforcements", *International Journal of Solids and Structures*, 45: 5419-5436.

Eshwar, N., Ibell, T., Nanni, A. (2003). "CFRP Strengthening of Concrete Bridges with Curved Soffits," Int. Conf. Structural Faults + Repair 2003, 1-3 July, Commonwealth Institute, London, UK. M.C. Forde, Ed., CD-ROM version, 10 pp.

Ferracuti, B., Savoia, M., Mazzotti, C. (2006). "A numerical model for FRP-concrete delamination". *Composites: Part B*, 37 (4-5): 356-364.

Foraboschi, P. (2004). "Strengthening of Masonry Arches with Fiber-Reinforced Polymer Strips", *Journal of Composites for Construction* ASCE, 8(3): 191-202.

Högberg, J.L. (2006). "Mixed mode cohesive law". *International Journal of Fracture*, 141: 549-559.

Kafkalidis, M.S., Thouless, M.D. (2002). "The effects of geometry and material properties on the fracture of single lap-shear joints". *International Journal of Solids and Structures*, 39: 4367-4383.

Li, S., Thouless, M.D., Waas, A.M., Schroeder, J.A., Zavattieri, P.D. (2006). "Mixed-mode cohesive-zone models for fracture of an adhesively bonded polymer-matrix composite". *Engineering Fracture Mechanics*, 73: 64-78.

Paggi, M. (2005). *Interface Mechanical Problems in Heterogeneous Materials*. PhD Thesis, Politecnico di Torino, Torino, Italy.

Tvergaard, V. (1990). "Effect of fiber debonding in a whisker-reinforced metal". *Materials Science and Engineering*, A125: 203-213.

Van den Bosch, M.J., Schreurs, P.J.G., Geers, M.G.D. (2006). "An improved description of the exponential Xu and Needleman cohesive zone law for mixed-mode decohesion". *Engineering Fracture Mechanics*, 73: 1220-1234.

Wriggers, P., Zavarise, G., Zohdi, T.I. (1998). "A computational study of interfacial debonding damage in fibrous composite materials". *Computational Materials Science*, 12: 39-56.

Xu, X.P., Needleman, A. (1993). "Void nucleation by inclusion debonding in a crystal matrix". *Modelling and Simulation in Materials Science and Engineering*, 1(2): 111-132.

Yuan, H., Teng, J.G., Seracino, R., Wu, Z.S., Yao, J. (2004). "Full-range behaviour of FRP-to-concrete bonded joints". *Engineering Structures*, 26: 553-565.

Zavarise, G. (1991). *Problemi termomeccanici di contatto - aspetti fisici e computazionali*, PhD Thesis, Università di Padova, Padova, Italy.

Table 1. Parameters used in the examples.

Example	E (GPa)	t (mm)	$p_{N\max}$ (MPa)	$p_{T\max}$ (MPa)	$g_{N\max}$ (mm)	$g_{T\max}$ (mm)	g_{Nu} (mm)	g_{Tu} (mm)
1	250	0.165	2	4	0.01	0.02	0.1	0.2
2, 3	250	0.165	2	16	0.01	0.06	0.1	0.6

Table 2. $F_{el,T}$, $F_{el,N}$ and F_{deb} for example 1 (case a1).

	$F_{el,T}$ (N/mm) (Eq. 28)	$F_{el,N}$ (N/mm) (Eq. 30)	F_{deb} (N/mm)	$F_{deb\max}$ (N/mm)	$L_{eff,deb}$ (mm) (Eq. 53)
r = 200 mm	57.6	400	180.1	182.1	96.0
r = 500 mm	57.5	1000	181.4	181.7	95.8
r = ∞	57.4	∞	181.7	181.7	95.8

Table 3. $F_{el,T}$, $F_{el,N}$ and F_{deb} for example 2 (case a2).

	$F_{el,T}$ (N/mm) (Eq. 28)	$F_{el,N} = F_{deb}$ (N/mm) (Eq. 30)
r = 150 mm	199.9	300
r = 200 mm	199.5	400
r = 250 mm	199.3	500

Table 4. $F_{el,T}$, $F_{el,N}$ and F_{deb} for example 3 (case b).

	$F_{el,T}$ (N/mm) (Eq. 28)	$F_{el,N} = F_{deb}$ (N/mm) (Eq. 30)
r = 50 mm	207.7	100
r = 75 mm	202.7	150
r = 100 mm	201.1	200

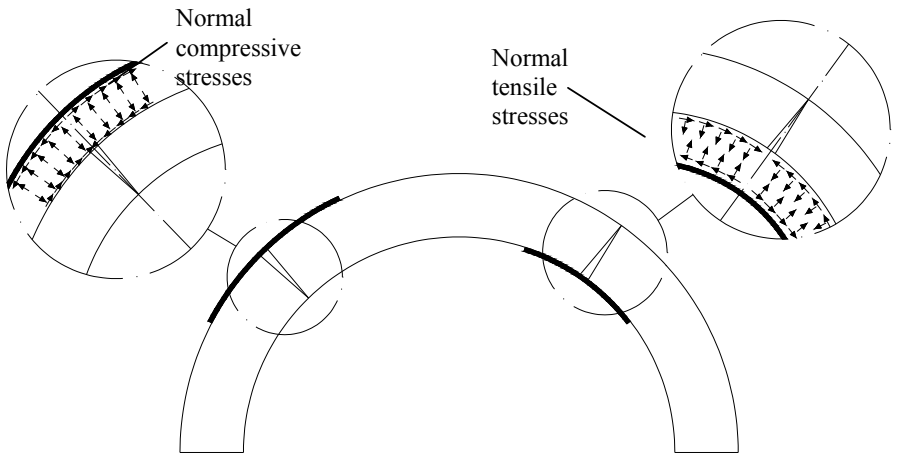

Figure 1. Interfacial stresses between FRP and curved masonry substrates.

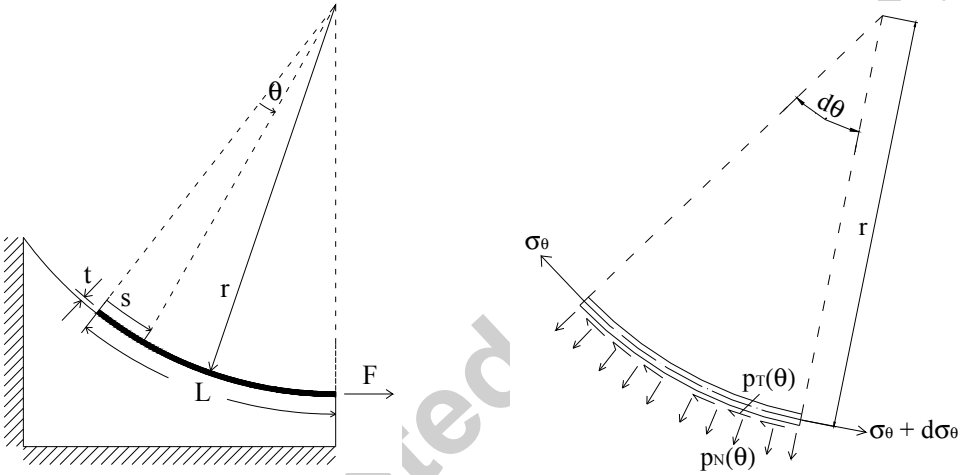

(a) Problem geometry (b) Differential element of the bonded plate

Figure 2. Problem definition.

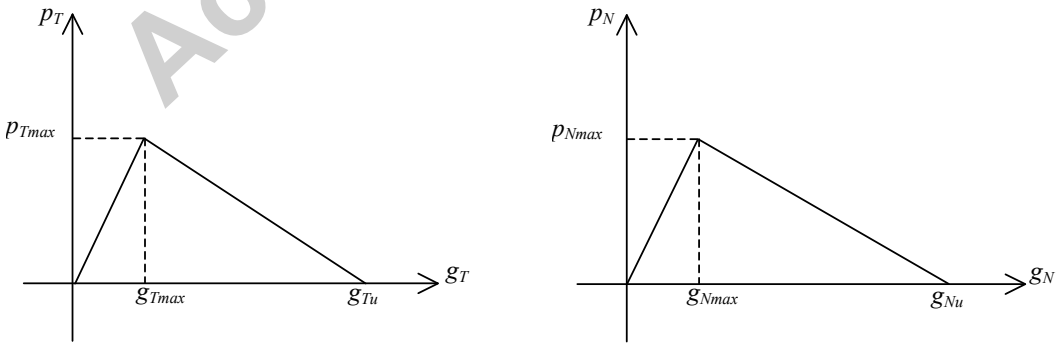

(a) Tangential direction (b) Normal direction under tension

Figure 3. Interfacial cohesive laws.

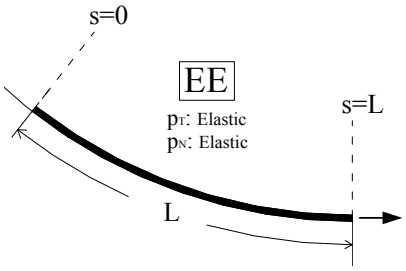

(a) EE stage (feasible)

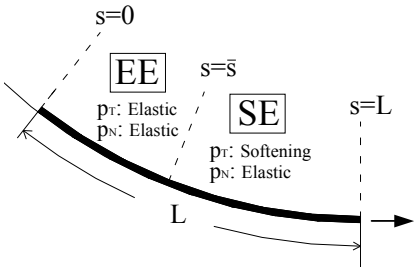

(b) EE-SE stage (feasible)

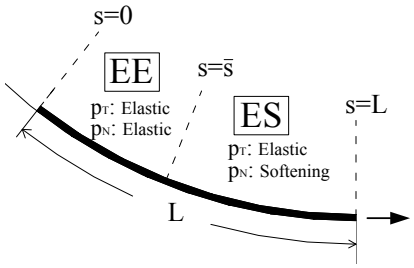

(c) EE-ES stage (not feasible)

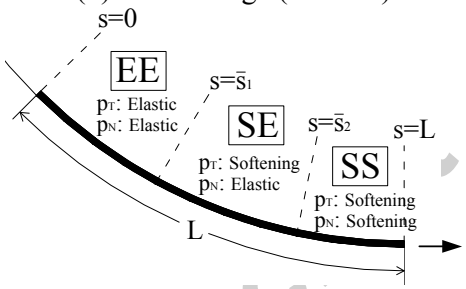

(d) EE-SE-SS stage (not feasible)

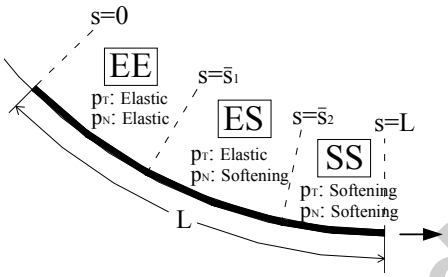

(e) EE-ES-SS stage (not feasible)

Figure 4. Stages in the behavior of the interface prior to debonding.

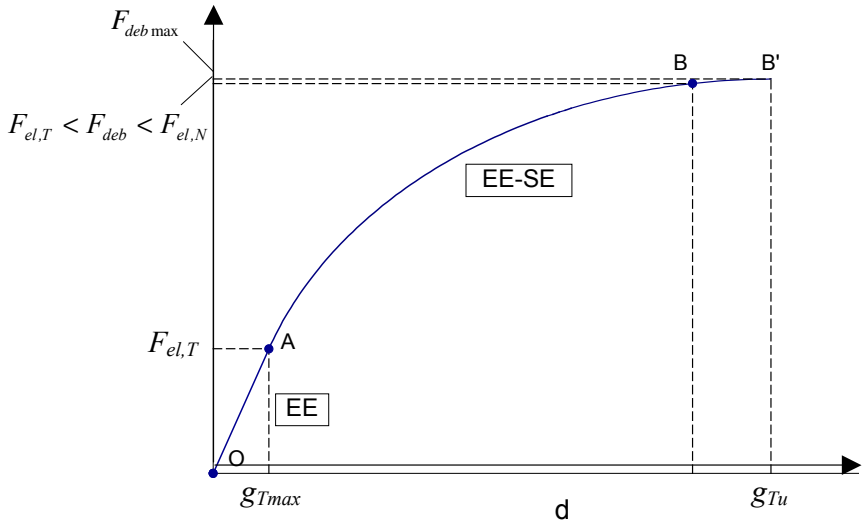

(a) Case a1

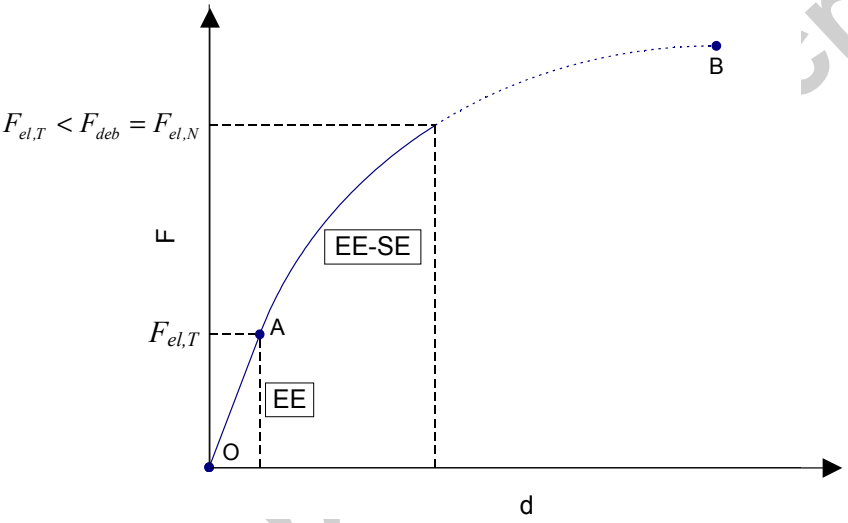

(b) Case a2

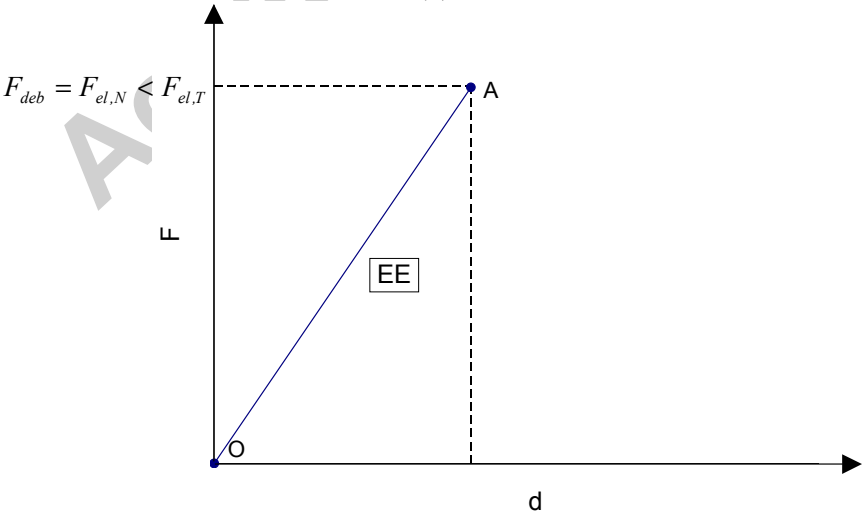

(c) Case b

Figure 5. Load-displacement curves prior to debonding.

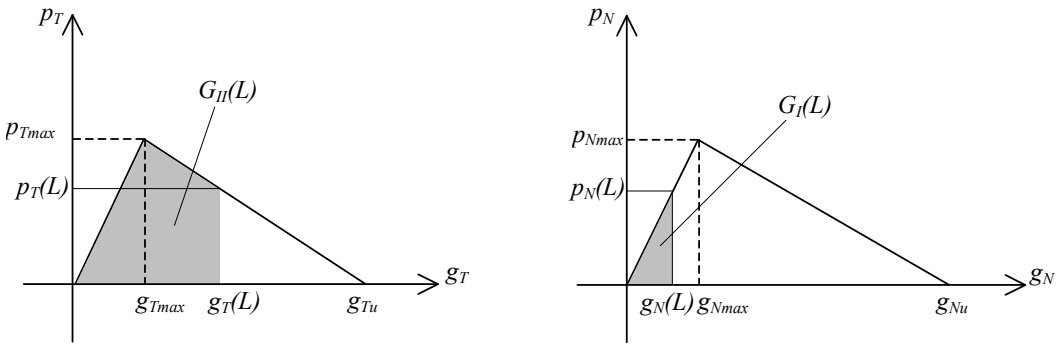

(a) Tangential direction (b) Normal direction under tension

Figure 6. Energy release rates during the EE-SE stage at the plate loaded end.

(a) $r = 200$ mm (b) $r = 500$ mm

Figure 7. Mesh used in the numerical analyses.

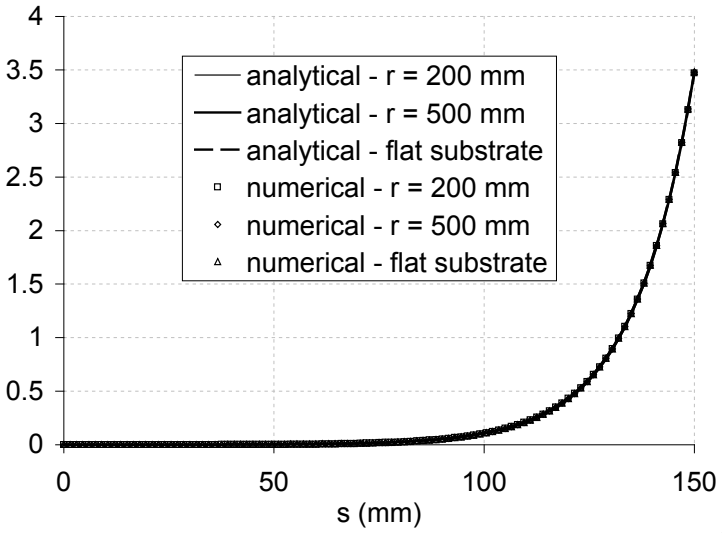

(a) Shear stresses

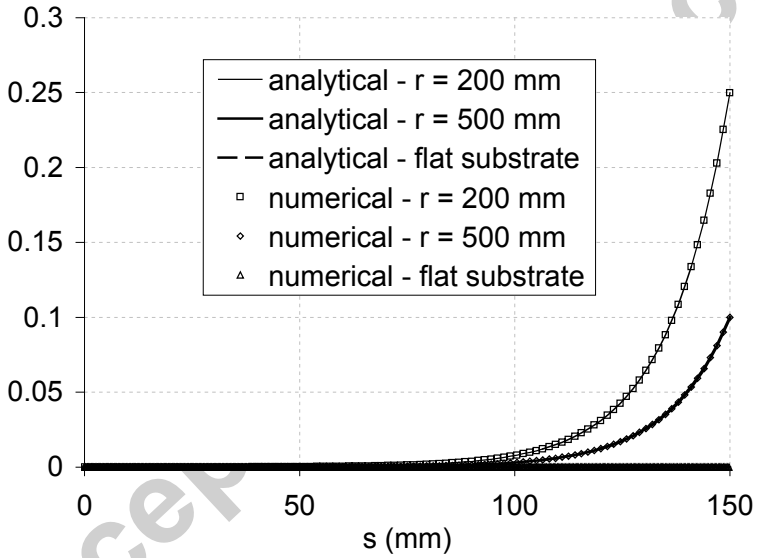

(b) Normal stresses

Figure 8. Example 1 (case a1): interfacial stresses – EE stage (F = 50 N/mm).

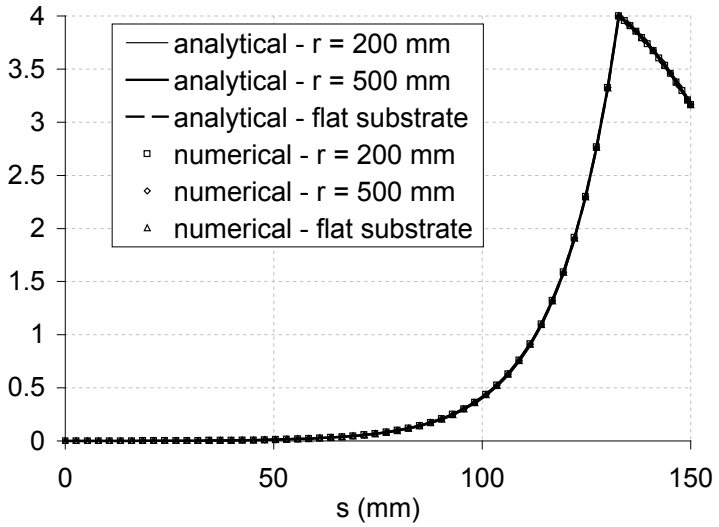

(a) Shear stresses

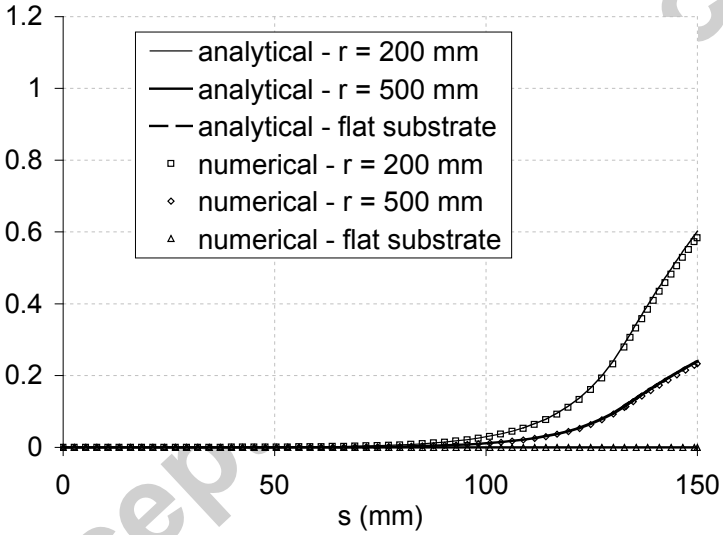

(b) Normal stresses

Figure 9. Example 1 (case a1): interfacial stresses – EE-SE stage (F = 120 N/mm).

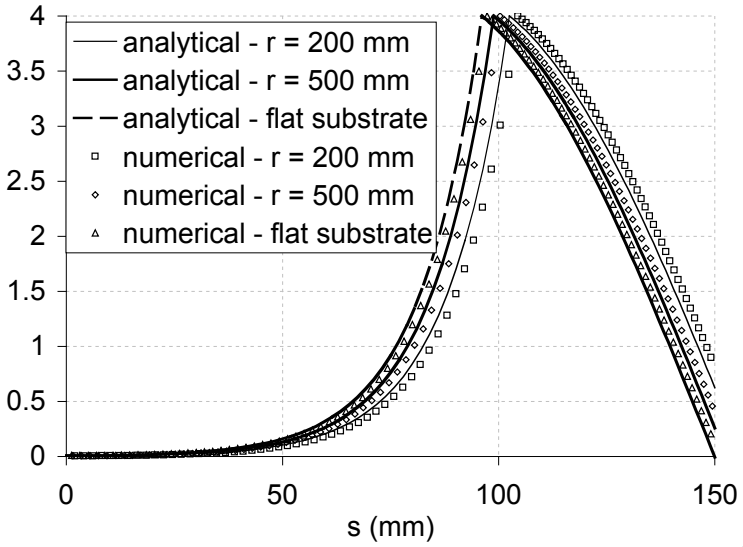

(a) Shear stresses

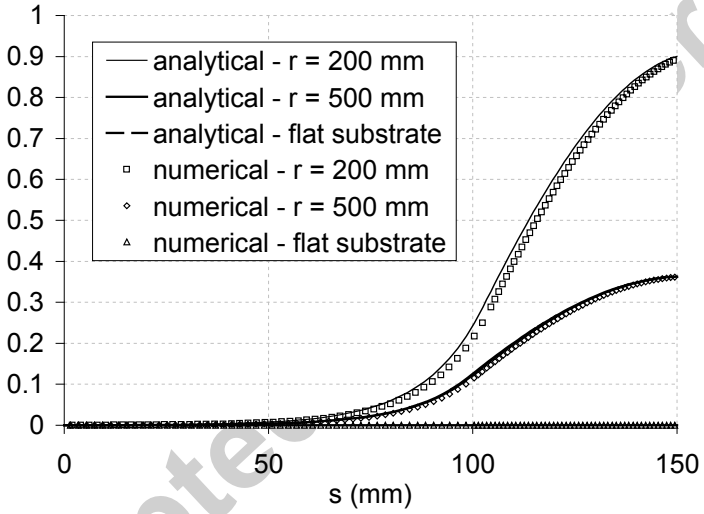

(b) Normal stresses

Figure 10. Example 1 (case a1): interfacial stresses – EE-SE stage at the initiation of debonding ($F = F_{deb}$).

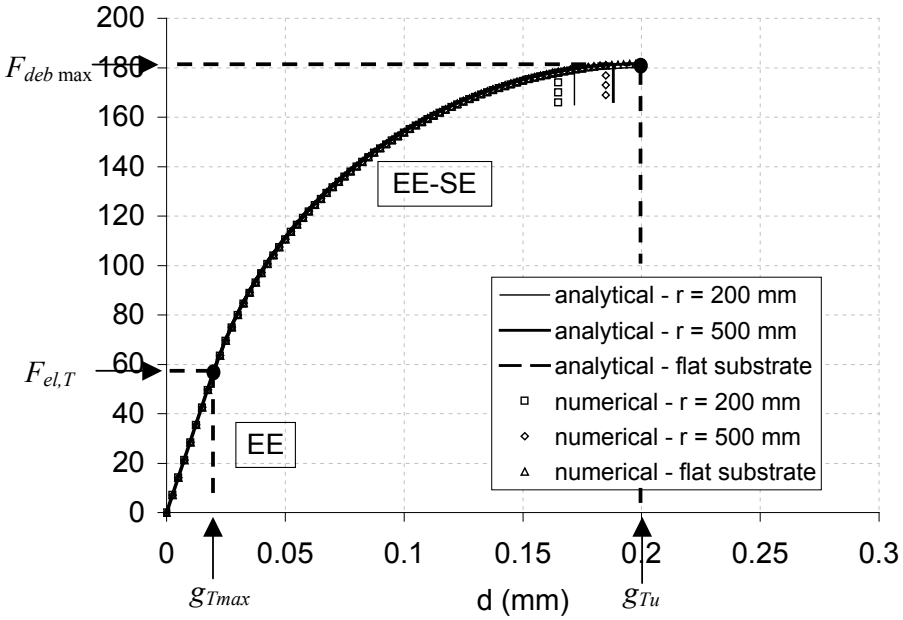

Figure 11. Example 1 (case a1): load vs. loaded-end displacement.

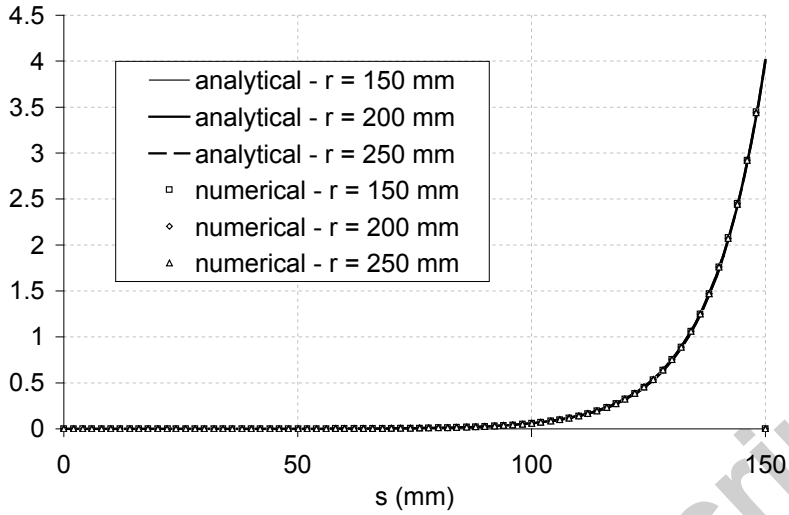

(a) Shear stresses

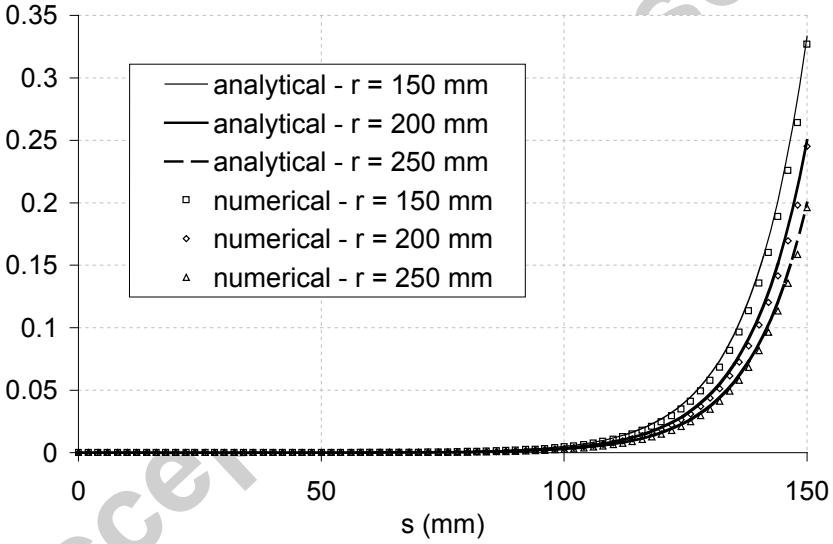

(b) Normal stresses

Figure 12. Example 2 (case a2): interfacial stresses – EE stage (F = 50 N/mm).

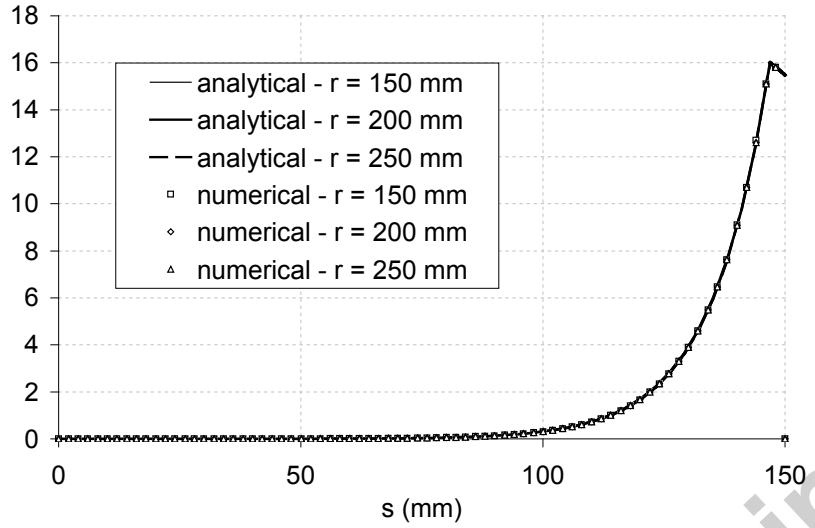

(a) Shear stresses

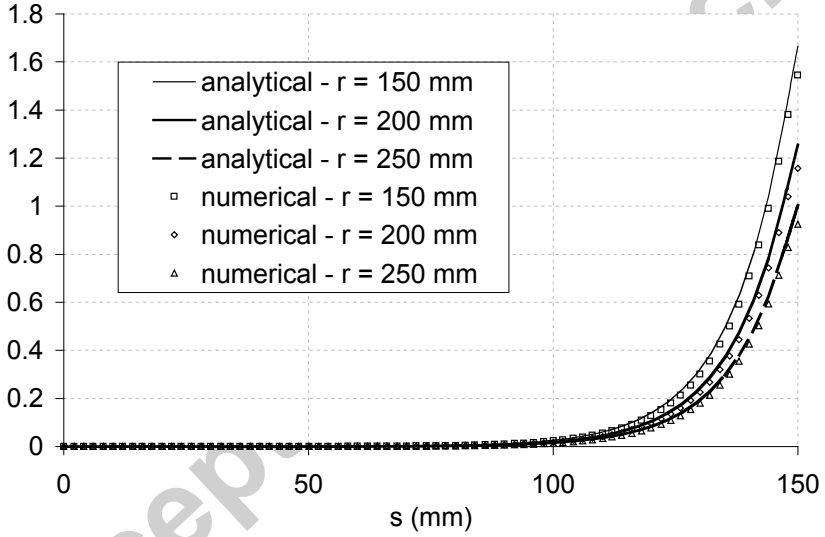

(b) Normal stresses

Figure 13. Example 2 (case a2): interfacial stresses – EE-SE stage (F = 250 N/mm).

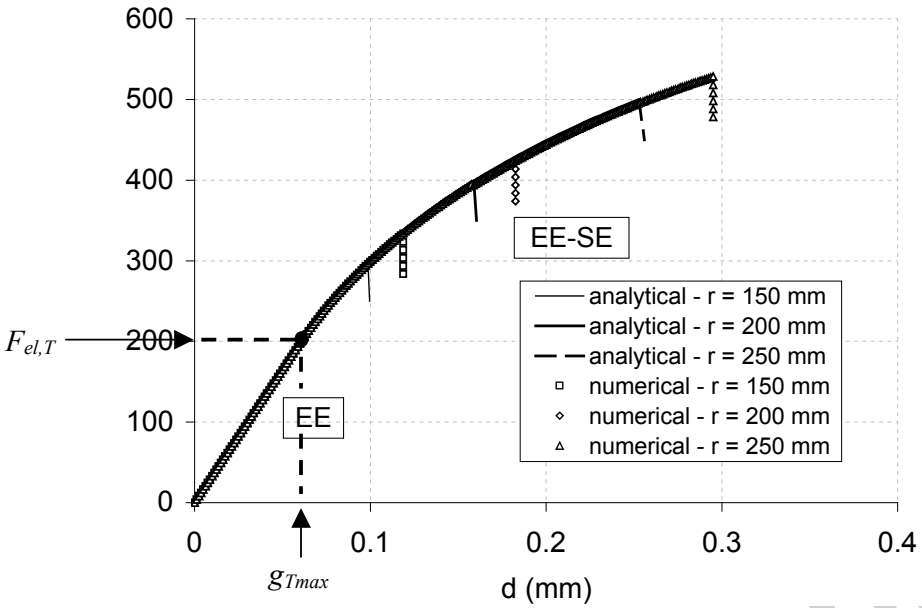

Figure 14. Example 2 (case a2): load vs. loaded-end displacement.

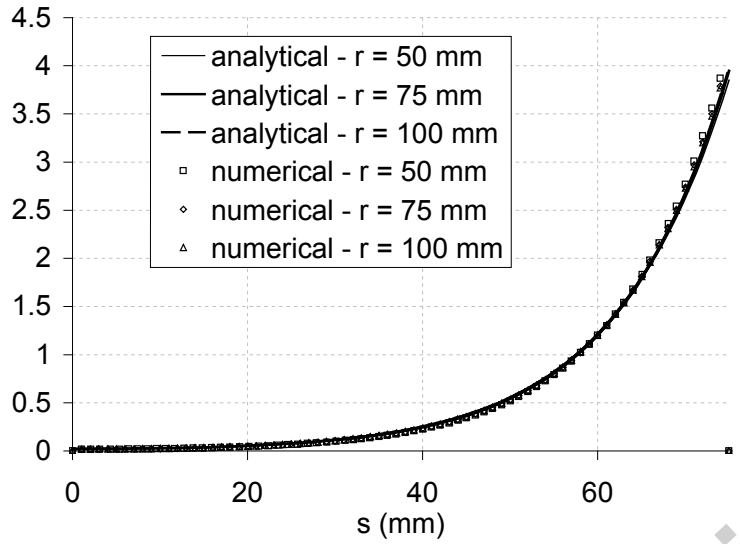

(a) Shear stresses

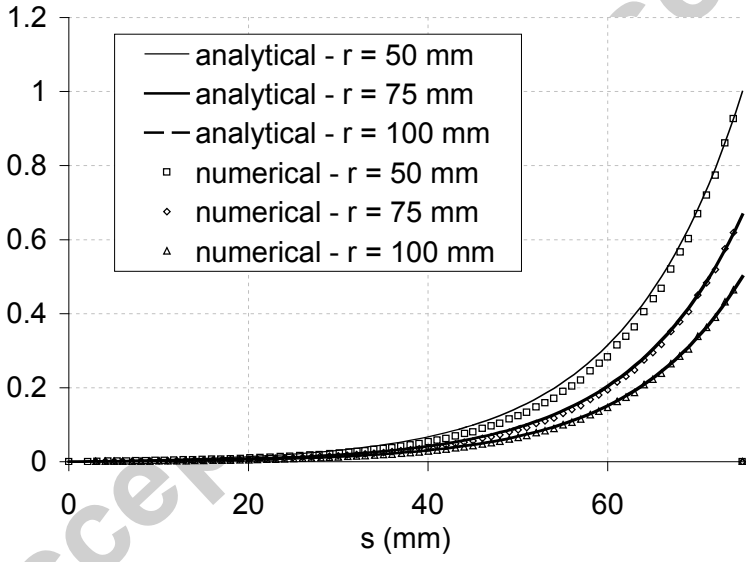

(b) Normal stresses

Figure 15. Example 3 (case b): interfacial stresses – EE stage (F = 50 N/mm).

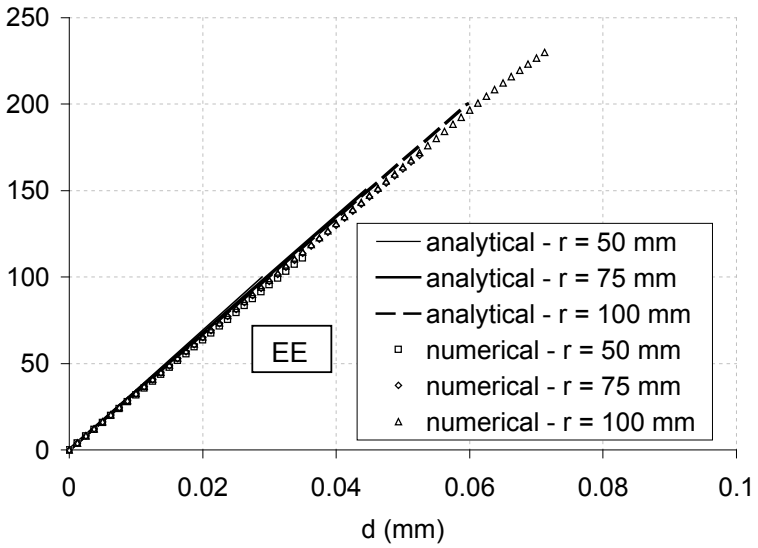

Figure 16. Example 3 (case b): load vs. loaded-end displacement.